POLITECNICO DI TORINO
Repository ISTITUZIONALE

# Dynamic Charge Redistribution as the Key Mechanism for NO2 Detection in MoS2 Revealed by In Operando Scanning Photoelectron Microscopy

*Original*
Dynamic Charge Redistribution as the Key Mechanism for NO2 Detection in MoS2 Revealed by In Operando Scanning Photoelectron Microscopy / Tomasi Cebotari, C., Gatsios, C., Mascia, A., Rühl, S., Vasquez, S., Pedrielli, A., Amati, M., Milosz, Z., Gregoratti, L., Risplendi, F., Re Fiorentin, M., Rossi, F., Nasi, L., Ligorio, G., List-Kratochvil, E.J.W., Verucchi, R., Pasquali, L., Petti, L., Cosseddu, P., Nardi, M.V., et al.. - In: ACS APPLIED MATERIALS & INTERFACES. - ISSN 1944-8244. - 18:30(2026), pp. 41889-41902. [10.1021/acsami.6c04862]

*Availability:*
This version is available at: 11583/3013234 since: 2026-07-17T10:10:57Z

*Publisher:*
American Chemical Society - ACS

*Published*
DOI:10.1021/acsami.6c04862

*Terms of use:*

This article is made available under terms and conditions as specified in the corresponding bibliographic description in the repository

*Publisher copyright*

(Article begins on next page)

25 October 2026

ACS APPLIED MATERIALS & INTERFACES

Open Access

This article is licensed under CC-BY 4.0

www.acsami.org

Research Article

# Dynamic Charge Redistribution as the Key Mechanism for $NO_2$ Detection in $MoS_2$ Revealed by *In Operando* Scanning Photoelectron Microscopy

Cristian Tomasi Cebotari,* Christos Gatsios, Antonello Mascia, Steffen Rühl, Sahira Vasquez, Andrea Pedrielli, Matteo Amati, Zygmunt Milosz, Luca Gregoratti, Francesca Risplendi, Michele Re Fiorentin, Francesca Rossi, Lucia Nasi, Giovanni Ligorio, Emil J.W. List-Kratochvil, Roberto Verucchi, Luca Pasquali, Luisa Petti, Piero Cosseddu, Marco Vittorio Nardi,* and Melanie Timpel*

Cite This: *ACS Appl. Mater. Interfaces* 2026, 18, 41889−41902

Read Online

ACCESS | Metrics & More | Article Recommendations | Supporting Information

**ABSTRACT:** Molybdenum disulfide ($MoS_2$) represents a promising candidate for low-power chemoresistive nitrogen dioxide ($NO_2$) sensing, and its potential for technological applications has generated considerable research interest. However, the sensing mechanism remains poorly understood, particularly regarding the type of $MoS_2$−$NO_2$ interaction and if morphology, defectivity, and thickness influence charge redistribution mechanisms. Therefore, we investigated $MoS_2$ thin films grown by ionized jet deposition (IJD), a technique suitable for large-area and industry-compatible fabrication, alongside exfoliated monolayer $MoS_2$ chemoresistors to elucidate the microscopic origin of $NO_2$-induced resistance changes. Using controlled gas sensing combined with *in operando* micro-focused X-ray photoelectron spectroscopy and scanning photoemission microscopy, we directly correlated resistance modulation with electronic structure variations, which is further supported by density functional theory calculations. Both atomically thin $MoS_2$ monolayers and nanostructured defect-rich IJD-$MoS_2$ thin films showed Mo 3d and S 2p core-level shifts to higher binding energies during $NO_2$ exposure, explained by local charge redistribution at the surface and modified core-level screening rather than net charge-transfer doping (i.e., transfer of free charge carriers into delocalized bands) and the associated band bending. In addition, IJD-$MoS_2$ thin films exhibited a transient Mo 3d component attributable to weak Mo−O bonding at defect sites, rather than from permanent oxidation. The additional component and core-level shifts were reversible upon $NO_2$ removal, evidencing a dynamic effect on the electronic structure. These results provide the first *in operando* insight into technologically scalable $MoS_2$ chemoresistors and establish design principles for $MoS_2$-based $NO_2$ sensing applications.

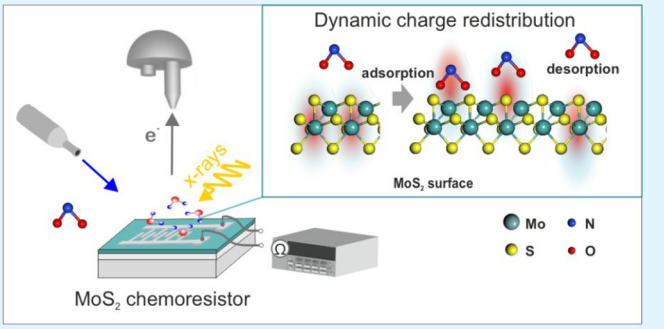


**KEYWORDS:** *molybdenum disulfide, in operando characterization, electronic properties of surfaces, chemical sensors, surface spectroscopies, transduction mechanisms*

## ■ INTRODUCTION

Two-dimensional (2D) transition-metal dichalcogenides offer strong potential for high-performance sensing of hazardous gases, such as carbon monoxide (CO), nitrogen oxides ($NO_x$), or sulfur dioxide ($SO_2$), because of their high surface activities, tunable electronic properties, and high surface-to-volume ratio, which favors a dramatic change in resistivity upon molecular adsorption.[1,2] Among them, molybdenum disulfide ($MoS_2$) stands out as sensing material due to its environmental stability and ability to operate at room temperature, which differentiates it from current metal-oxide technologies requiring high operating temperatures (>200 °C) to initiate gas-sensing processes (adsorption/desorption).[3,4] This not only increases fabrication complexity but also results in high power consumption. Although alternative low-power sensing platforms based on other materials such as carbon nanotubes are being explored,[5−7] $MoS_2$ allows the use of a wide range of growth

Received: March 9, 2026
Revised: June 29, 2026
Accepted: July 3, 2026
Published: July 13, 2026

Downloaded from pubs.acs.org/aamick/article-pdf/18/30/41889/65852670/am-2026-04862n.pdf by POLITECNICO DI TORINO user on 22 October 2026



© 2026 The Authors. Published by American Chemical Society

methods, including chemical vapor[8] and pulsed laser [9,10] deposition, sputtering,[11,12] ionized jet deposition (IJD),[13,14] and wet-chemical methods,[15,16] producing films with distinct morphologies, varying crystallinity, and a broader distribution of defects.

Previous studies[17,18] have shown that $MoS_2$ surfaces respond efficiently to nitrogen dioxide ($NO_2$), which is particularly relevant because of its widespread presence in urban and industrial environments and its harmful impact on human health.[19−21] Early investigations showed that few-layer $MoS_2$ exhibited significant resistance increases upon exposure to $NO_2$ concentrations as low as 500 ppb.[22] Other studies have revealed that sensitivity and recovery behavior depend strongly on the material's thickness, substrate interactions, doping level, and sulfur vacancies.[3,23] For example, defect-rich $MoS_2$ nanosheets exhibit high $NO_2$ responses,[24] while doping approaches involving the incorporation of hetero-atoms into the $MoS_2$ lattice can further modulate adsorption kinetics and charge-transfer (i.e., spatial charge redistribution) efficiencies.[25,26]

Direct experimental observation of the electronic response of the sensing layer during gas exposure remains limited. *In operando* spectroscopic approaches are therefore essential to correlate electrical sensing signals with changes in the electronic structure at the surface. Variations in conductivity are most often attributed to surface chemistry, such as charge transfer with adsorbed species, which can change the surface electronic character from n-type to p-type,[27] as well as defect-mediated chemisorption.[28] Modulations of the grain-boundary energy barrier upon gas exposure represent another possible contribution, while device-related factors, such as changes in contact resistances can also have a considerable effect.[3,23] Density functional theory (DFT) calculations predict strong electron-withdrawing interactions between $NO_2$ and $MoS_2$, especially at defective sites,[29−32] but verifying these predictions under operational conditions requires techniques capable of probing the chemical structure during gas adsorption.

*In situ* and *in operando* spectroscopic techniques have enabled direct observation of gas-induced changes in electronic structure.[33−35] Scanning photoelectron microscopy (SPEM) studies of $NO_x$ adsorption on monolayer $MoS_2$ exfoliated onto hexagonal boron nitride (hBN) have reported Mo 3d core-level shifts toward lower binding energy, interpreted in terms of electron transfer from $MoS_2$ to the electron accepting $NO_x$ molecules.[36] Within this framework, the observed binding energy shift corresponds to changes of the local surface electrostatic potential, analogous to upward band bending and the depletion of electrons in $MoS_2$. This electrostatic description is commonly used to account for the effect of charge transfer in semiconductors, including metal oxides[37] and carbon nanotubes.[6] Near-ambient-pressure X-ray photoelectron spectroscopy (NAP-XPS) allows to directly correlate surface adsorption with the electrical response of 2D materials under realistic gas environments. For example, Minezaki et al.[38] performed in operando NAP-XPS under $H_2$ dosing while monitoring resistance changes in a $WS_2$ chemoresistor. These approaches represent powerful tools for distinguishing modulation of the active material under device operation for identifying the contributions of reversible physisorption versus defect-driven chemisorption.

These methodological advances enable us to explore the lack of knowledge on the sensing mechanism of monolayer (ML) $MoS_2$ and thin films. Here we present the analysis of chemoresistive sensors that served us as representative sensing systems: one employing pristine exfoliated ML-$MoS_2$ representing an atomically thin and smooth surface,[39] and one based on a nanostructured IJD-$MoS_2$ thin film representing a rough and defect-rich MoS2 surface. The formation of interconnected nanostructures in IJD-grown $MoS_2$ films with enhanced roughness and defect-rich morphologies has been demonstrated in our previous studies.[13,40] The differences between ML-$MoS_2$ (i.e., atomically flat surface with low defect density) and IJD-grown $MoS_2$ (i.e., defect-rich nanostructured thin films) make them ideal model systems for investigating if morphology, roughness, and defectivity strongly influence chemoresistive transduction. Both ML and IJD-MoS2 were integrated into a technologically relevant chemoresistor architecture, fabricated with silver screen-printed interdigitated electrodes (IDEs) on a $SiO_2$ substrate. Ag screen-printed IDEs were selected for their simplicity and scalability in large-area production, whereas the $SiO_2$ substrate provides excellent electrical insulation and represents a well-known reference substrate in various technological applications. Although identical in chemical composition, these ML and IJD-MoS2 exhibit fundamentally different morphologies, defect densities, crystalline qualities, and thicknesses and can be considered as extreme cases regarding its $MoS_2$−$NO_2$ interaction. By combining dynamic resistance measurements with *in operando* micro-focused XPS and SPEM we directly probed $NO_2$-induced core-level shifts in the active IDE spacing region and correlated them to the measured resistance modulation. Upon $NO_2$ exposure, the Mo 3d and S 2p core levels shifted toward higher binding energies, concomitant with an increase in the chemoresistor resistance. After evacuation of the gas, the core-level binding energies revert toward their initial values, accompanied by recovery of the electrical response. This integrated analysis clarified how surface charge redistribution, defect interactions, and conduction pathways govern the distinct sensing behaviors of exfoliated and IJD-grown $MoS_2$. The resulting insights establish mechanistic guidelines for the rational design of scalable and cost-efficient $MoS_2$-based gas sensors bridging ideal 2D materials and technologically relevant thin films.

## ■ EXPERIMENTAL SECTION

### Device Fabrication

Ag IDE were patterned on Si/$SiO_2$ substrates (300 nm oxide) by screen printing with a semi-automatic Aurel C290 printer and a stainless-steel mesh. After printing, the Ag contacts were cured at 110 °C for 15 min in an oven. Two types of $MoS_2$-based chemoresistive devices were subsequently prepared. The first device type is based on a single-crystalline monolayer of $MoS_2$ (ML-$MoS_2$), fabricated using a thermally activated Au-mediated exfoliation method described previously,[41] while the second device type employs IJD−grown $MoS_2$ (IJD-$MoS_2$) as the sensing material.

For the ML-$MoS_2$ device, IDE included 10 fingers with a width of 300 μm and IDE spacing of 300 μm. The ML exfoliation was done on top of fresh gold substrates prepared by depositing a 200 nm thick Au film onto Si wafers via thermal evaporation, attaching a glass support with UV-curable epoxy, and template-stripping the metal film to expose a clean, oxide-free Au surface immediately before use. Synthetic $MoS_2$ crystals were cleaved using Kapton tape and the freshly cleaved surface was pressed onto the template-stripped Au. The sample was placed on a hotplate and annealed in ambient conditions at 200 °C for 120 s, which activated the exfoliation process. After annealing, the substrate was briefly cooled for approximately 15 s and the tape was then peeled off, leaving behind large-area single-layer $MoS_2$ regions on gold (major axis of more than 1 cm). The $MoS_2$ monolayer was

Downloaded from pubs.acs.org/aamick/article-pdf/18/30/41889/65852670/am-2026-04862n.pdf by POLITECNICO DI TORINO user on 22 October 2026



https://doi.org/10.1021/acsami.6c04862
ACS Appl. Mater. Interfaces 2026, 18, 41889−41902

then transferred onto the pre-patterned substrate using a wet-transfer method,[41] ensuring complete bridging of the inter-electrode region.

For the IJD-$MoS_2$ device, IDE consisted of 16 fingers, each 200 μm wide with 150 μm IDE spacing. $MoS_2$ deposition was performed using IJD system operated at an accelerating voltage of 18 kV and a pulse frequency of 40 Hz. The substrate temperature was maintained at 300 °C throughout the deposition. The resulting film thickness was approximately 500 nm.

The two devices employed slightly different IDE geometries due to practical fabrication and substrate availability constraints during device preparation. While differences in IDE spacing and number may influence the absolute resistance and response magnitude, the present work mainly focuses on correlating the *in operando* electrical behavior with the simultaneous XPS-observed electronic structure modifications under $NO_2$ exposure, rather than on a strict quantitative comparison of sensing performance between the two device architectures.

## Electron Microscopy Imaging

Scanning electron microscopy (SEM) imaging of the chemoresistors was carried out using a Thermo Scientific Helios 5 PFIB CXe instrument. Images were acquired at normal incidence and at a 54° tilt angle using secondary electrons, and for high resolution through-the-lens detectors (TLD) and immersion mode were used. Acceleration voltage and working distance were set according to instrument guidelines to optimize surface contrast and minimize charging. A cross-sectional transmission electron microscopy (TEM) sample of the IJD-$MoS_2$ thin film was prepared through a standard lift-out procedure. Final polishing was carried out with $Xe^+$ ions from the FIB source at 30 kV and 1.0−0.1 nA, using an overtilt angle of 1°. TEM characterization was performed on a field-emission JEM-2200FS JEOL TEM (JEOL Ltd., Tokyo, Japan) equipped with an in-column Omega filter and operated at 200 kV.

## Gas Sensing Setups in $N_2$ and UHV

Gas sensing experiments in $N_2$ atmosphere were performed in a custom-made gas chamber[42] equipped with two independent sample holders, enabling simultaneous operation of ML-$MoS_2$ and IJD-$MoS_2$ under identical environmental conditions, i.e., at room temperature (RT) and atmospheric pressure.

Certified $NO_2$ gas (30 ppm) was supplied through mass-flow-controlled lines. Two independent flowmeters regulate the $NO_2$ and $N_2$ streams, maintaining the total flow at 450 mL/min. The $NO_2$ concentrations delivered to the devices were in the 3−13 ppm range and were calculated as:

$$[NO_2]_{chamber} = \frac{\phi_{NO_2}}{\phi_{tot}} \times [NO_2]_{bottle}$$

where $[NO_2]_{chamber}$ is the expected concentration of $NO_2$ inside of the gas sensing chamber, $[NO_2]_{bottle}$ is the concentration inside of the $NO_2$ gas bottle and $\phi_{NO_2}/\phi_{tot}$ are the fluxes (in mL/min) of the $NO_2$ line and the total flux (given by the sum of the $NO_2$ and carrier $N_2$ fluxes). This formulation accounts for the dilution of the $NO_2$ source gas by the carrier $N_2$ flow, providing an accurate estimation of the effective $NO_2$ concentration reaching the sample surface. The measurement protocol involved a 10-min $NO_2$ injection phase, during which the sensors were exposed to the reactive gas mixture, followed by a 20-min flushing period in pure $N_2$ to promote recovery of the baseline resistance.

Electrical measurements were performed using two Keithley Series 2600B in four-wire configuration under a constant 1 V bias.

Dynamic high pressure (DHP) dosing of $NO_2$ under UHV conditions at the ESCA Microscopy beamline (Elettra−Synchrotron Trieste, Italy) was done via a stainless-steel poppet valve positioned a few millimeters above the sample,[35] delivering reproducible local dosing pulses at a frequency of 0.3 Hz and valve opening time of 2.42 ms that raised the chamber pressure up to $\sim 1 \times 10^{-5}$ mbar during gas exposure. According to the previous work of Amati et al.,[43] it is reasonable to assume that a 2.42 ms delivers approximately 100 mbar on the surface of the chemoresistors, leading to a nominal $NO_2$ concentration of ∼8 ppm. From these assumptions we can calculate the impingement rate as:

$$Z = \frac{P}{\sqrt{2\pi m k_B T}} \left[\frac{\text{molecules}}{\text{m}^2\text{s}}\right]$$

where $P$ is the pressure on the chemoresistor surface during each pulse, $m$ is the $NO_2$ molecule mass ($m = 7.64 \times 10^{-26}$ kg), $k_B$ is the Boltzmann constant, and $T$ is the temperature assumed to be 300 K. We can evaluate the number of molecules arriving on the chemoresistors per pulse by multiplying the impingement rate by the aperture time obtaining:

$$N_{pulse} = Z\Delta t_{ap} = 8.13 \times 10^{19} \left[\frac{\text{molecules}}{\text{cm}^2}\right]$$

where $\Delta t_{ap}$ is the aperture time (2.42 ms). Given the very high number of arriving molecules per pulse with respect to available adsorption sites ($\sim 10^{18}$ [molecules/cm$^2$]), we can assume that in the saturation regime, i.e., dosing for >20 min, the chemoresistor surface is fully covered by $NO_2$ molecules.

Note that the gas sensing experiments in $N_2$ and UHV were done without reaching saturation and baseline recovery (i.e., no induced thermal recovery), since the scope was to qualitatively compare the electrical sensing response of the chemoresistors to $NO_2$ under different environments ($N_2$ vs UHV). The selectivity of IJD-$MoS_2$ toward typical target gases was evaluated through an extended gas response curve to ammonia ($NH_3$), $NO_2$, and carbon dioxide ($CO_2$), reported in Figure S1 (Supporting Information), which highlights its preferential response to $NO_2$. *In operando* spectroscopy during $NO_2$ exposure (see below) was performed in the saturation regime, i.e., $NO_2$ exposure >20 min to ensure complete chemical reactivity before XPS/SPEM data acquisition.

Electrical characterization was performed simultaneously via a Keithley 2612B source-measure unit operated in two-wire mode at 1 V.

## *In Operando* XPS and SPEM Analysis

*In operando* XPS and SPEM were carried out at the ESCA Microscopy beamline (Elettra−Sincrotrone Trieste, Italy). Samples were mounted on grounded holders and loaded into an ultrahigh-vacuum (UHV) chamber with a base pressure of $\sim 1 \times 10^{-9}$ mbar.

Core-level spectra (Mo 3d, S 2s, and S 2p) were collected using monochromatic synchrotron radiation with photon energy of 647.7 eV and a hemispherical analyzer, providing an overall energy resolution of ∼180 meV. The photon beam for high-resolution XPS measurements had a spot size of approximately 75 μm. SPEM maps were acquired using a micro-focused beam with ∼7 μm lateral resolution. To avoid extensive beam-induced damage due to the high photon flux, single-pixel spectra were collected using a dwell time of 30 ms. Consecutive SPEM maps were taken moving the region of interest to adjacent positions to avoid the presence of beam induced effects.

Reference spectra were collected with the bias already applied to account for bias-induced spectral shifts. Since $MoS_2$ directly contacted the Ag electrodes in both device architectures, the applied voltage predominantly dropped across the $MoS_2$.

## Data Processing

XPS spectra were normalized in intensity to the main Mo 3d or S 2p core level components to enable a good visibility of the BE shifts. Mo 3d and S 2s core levels are deconvoluted using Voigt components. An active Shirley background is used to account for secondary-electron contributions to the photoelectron intensity.[44] The spectra were

Downloaded from pubs.acs.org/aamick/article-pdf/18/30/41889/65852670/am-2026-04862n.pdf by POLITECNICO DI TORINO user on 22 October 2026



https://doi.org/10.1021/acsami.6c04862
ACS Appl. Mater. Interfaces 2026, 18, 41889−41902

aligned by calibrating to C 1s core level spectra when required to correct for residual charging.

The absence of beam-induced material modification and/or damage, which has been shown to strongly depend on sample quality and substrate,[45,46] was assessed by comparing XPS scans in sequence of Mo 3d and S 2p core levels on both chemoresistors, shown in Figures S2 and S3 (Supporting Information). The presence of $NO_2$ on the chemoresistors' surface during DHP was confirmed by acquiring high-resolution XPS spectra in the N 1s core level region before, during and after $NO_2$ dosing on both chemoresistors (Figure S4, Supporting Information).

## Computational Methods

DFT calculations were performed within the plane-wave implementation of Quantum Espresso,[47,48] using the rev-vdW-DF2 exchange-correlation functional[49] and norm-conserving pseudopotentials.[50] All calculations were spin-polarized to properly describe the open-shell $NO_2$ molecule. A kinetic energy cutoff of 75 Ry for the wavefunctions and 300 Ry for the charge density were used. Adsorption was modeled using 5 × 5 supercells with a 20 Å vacuum region to avoid spurious interactions between periodic replicas, and dipole corrections are applied to remove artificial electric fields along the surface normal. Brillouin zone sampling was performed at Γ, and convergence with respect to k-point sampling/supercell size was verified for representative configurations.

Charge redistribution upon adsorption was analyzed through Bader partitioning.[51]

Core-level binding energies (Mo 3d and S 2p) were computed within the ΔSCF framework using half core-hole pseudopotentials generated with ONCVPSP,[52] following the Slater transition-state approach.[53] The vacuum level was obtained from the planar-averaged electrostatic potential in the middle of the vacuum region (with dipole correction), enabling a consistent reference for core-level shifts across configurations. Binding energies (BE) were obtained from total energy differences and referenced consistently to the vacuum level, allowing for a direct comparison of core-level shifts between different adsorption configurations. Mo 3d and S 2p core level BE shifts due to interaction were calculated as $\Delta BE = BE_{NO2} - BE_{pristine}$, where $BE_{NO2}$ is the BE resulting from the interacting system and $BE_{pristine}$ is the one of the non-interacting system. For the interacting (non-interacting) system Mo and S atoms right below (far away from) the $NO_2$ molecule were chosen.

## ■ RESULTS

In Figure 1a, the optical micrograph of the ML-$MoS_2$ device is shown, taken with polarized light to emphasize the contrast of the large-area monolayer (brown). The SEM image in Figure 1b displays the part of the IDEs (top and bottom of the micrograph) where the corresponding IDE spacing of ∼250 μm can be clearly seen. Figure 1c,d show magnified SEM images tilted by 54° in the center of the IDE spacing. The ML-$MoS_2$ exhibits the smooth surface typical of a

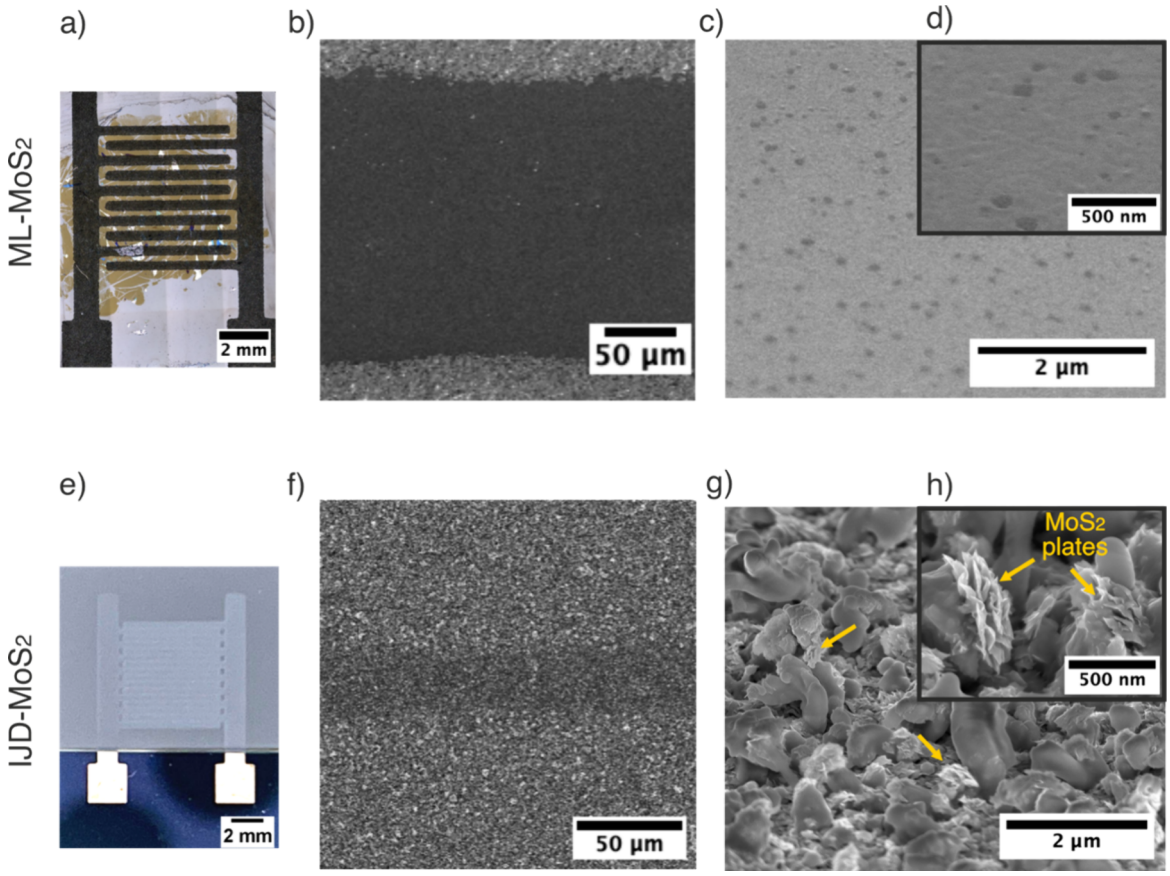


**Figure 1.** (a) Optical micrograph taken with polarized light of the ML-$MoS_2$ chemoresistor; (b−d) SEM images in between the IDE spacing of the ML-$MoS_2$ chemoresistor: (b) top view, (c, d) 54° tilted views with higher magnifications; (e) optical micrograph of the IJD-$MoS_2$ chemoresistor; (f−h) SEM images in between the IDE spacing of IJD-$MoS_2$ chemoresistor: (f) top views, (g, h) 54° tilted view with higher magnification showing plate-like $MoS_2$ structures.



https://doi.org/10.1021/acsami.6c04862
ACS Appl. Mater. Interfaces 2026, 18, 41889−41902

Downloaded from pubs.acs.org/aamick/article-pdf/18/30/41889/65852670/am-2026-04862n.pdf by POLITECNICO DI TORINO user on 22 October 2026

monolayer with some crater-like defects (dark dots), most likely arising from the exfoliation procedure.

Figure 1e presents an optical micrograph of the IJD-$MoS_2$ chemoresistor, showing the device layout and the uniform coverage of the active material across the IDEs. In Figure 1f, the SEM image acquired across the IDE spacing highlights bright spots evenly distributed across the entire surface. Figure 1g provides a magnified SEM view, acquired at a 54° tilt, revealing the complex three-dimensional morphology of IJD-$MoS_2$, namely large round-shaped agglomerates extending upward from the surface, and adjacent plate-like $MoS_2$ structures exhibiting the 2H-$MoS_2$ phase (visible in the cross-sectional TEM view in Figure S5) as indicated by the arrows (Figure 1g,h). This morphology is in agreement with the one observed for IJD-$MoS_2$ thin films grown under similar conditions,[54] i.e., *in situ* annealing at 300 °C during deposition.

To test the resistance behavior, the chemoresistors were introduced in a custom-built gas chamber, a constant bias of 1 V was applied for the resistance readout. Figure 2 shows the evolution of the resistance change over time for both ML-$MoS_2$ and the IJD-$MoS_2$ chemoresistors. The measurements were carried out in the dark at RT during controlled exposure to $NO_2$ gas under $N_2$ atmosphere. The chemoresistors display different baseline resistances, with ML-$MoS_2$ showing a baseline in the MΩ range, whereas IJD-$MoS_2$ displays a much lower baseline resistance in the Ω range. This significantly reduced resistance in IJD-$MoS_2$ is consistent with its higher intrinsic conductivity, as demonstrated in previous work.[13,40] In particular, $MoS_2$ deposited via IJD has been shown to exhibit a valence band (VB) onset closer to the Fermi level, indicating enhanced carrier density and improved electronic transport, which directly accounts for the lower baseline resistance observed here.

Both chemoresistors exhibit an increase in resistance upon $NO_2$ exposure. The ML-$MoS_2$ shows a higher resistance increase compared to the IJD-$MoS_2$ for the same concentrations. Both sensors respond proportionally to the increasing concentration. Notably, the IJD-$MoS_2$ chemoresistor additionally demonstrates preferential selectivity toward $NO_2$ over other common interfering gases. As shown in Figure S1 (Supporting Information), exposure to $NH_3$ and $CO_2$ at comparable concentrations produces negligible resistance changes relative to the strong response observed upon $NO_2$ injection, confirming the sensor's selectivity for $NO_2$ detection.

In both cases, the passive recovery after exposure remains incomplete within the 20-min flushing interval, indicating that desorption of $NO_2$ molecules from the $MoS_2$ surface is relatively slow at room temperature and pressure, as previously reported on pristine $MoS_2$.[17]

Figure 3 presents the resistance variation of both $MoS_2$ chemoresistors recorded during $NO_2$ dosing in UHV in the dynamic regime (i.e., no saturation and recovery reached). The resistance change in the ML-$MoS_2$ chemoresistor is shown in Figure 3a, while Figure 3b displays the corresponding data for the IJD-$MoS_2$ chemoresistor. In both cases, a clear and reproducible increase in resistance is observed upon $NO_2$ exposure.

The increase of resistance for both chemoresistors when exposed to $NO_2$ in $N_2$ atmosphere and under UHV conditions suggests comparable chemical reactivity in both environments.

Figure 4 shows spatially resolved SPEM images corresponding to the photoemission intensity of the Mo 3d core level before $NO_2$ exposure. These images are a convolution of the chemical and topographical contrast of the surface. Since these images were collected from chemically uniform surfaces, that of ML-$MoS_2$ and IJD-$MoS_2$ uniformly covering the device, the visible contrast is attributed mainly to topographical effects and allows to clearly identify the different surface regions of the device.

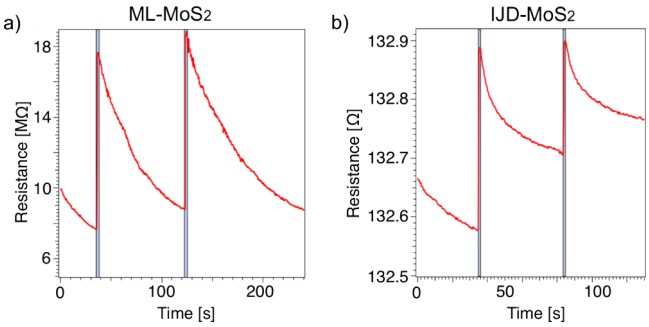


**Figure 3.** Resistance measurements (dynamic regime) of (a) ML-$MoS_2$ and (b) IJD-$MoS_2$ chemoresistors in UHV upon $NO_2$ dosing (0.3 Hz valve repetition and 2.42 ms aperture).

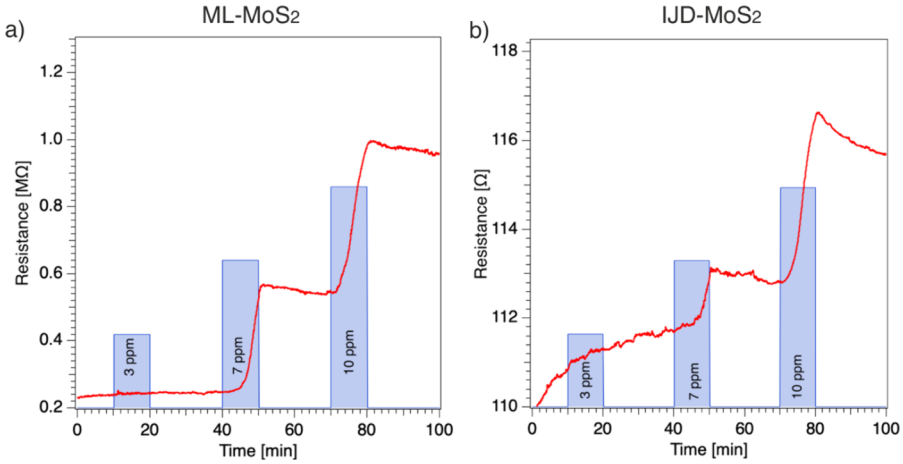


**Figure 2.** Resistance measurements (dynamic regime) while sensing $NO_2$ of different concentrations (3−13 ppm) in $N_2$ atmosphere at room temperature for (a) ML-$MoS_2$ and (b) IJD-$MoS_2$ chemoresistors.



https://doi.org/10.1021/acsami.6c04862
ACS Appl. Mater. Interfaces 2026, 18, 41889−41902

Downloaded from pubs.acs.org/aamick/article-pdf/18/30/41889/65852670/am-2026-04862n.pdf by POLITECNICO DI TORINO user on 22 October 2026

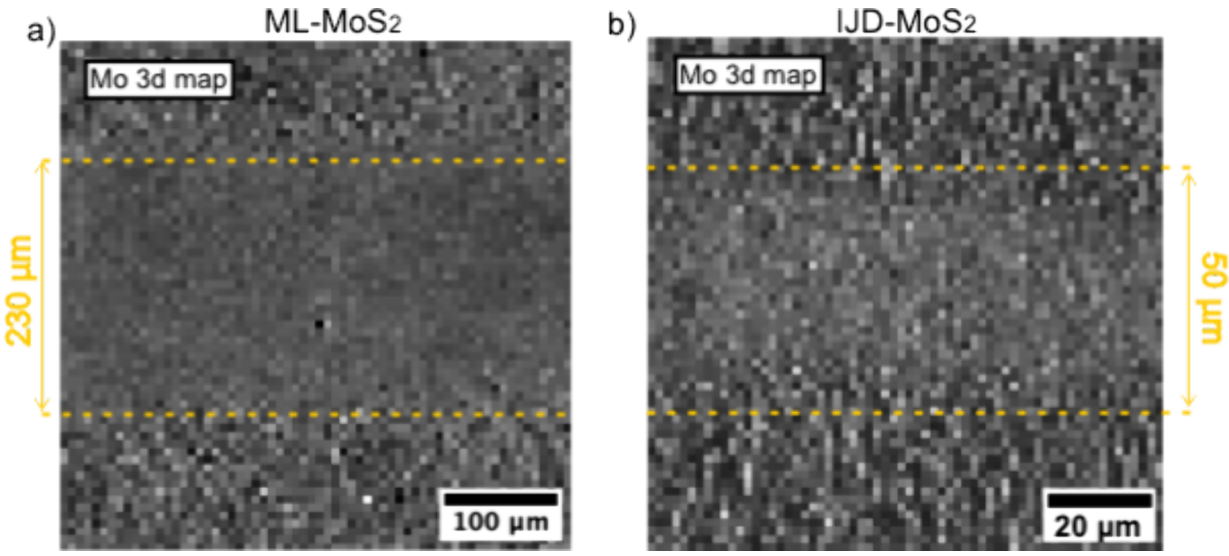


**Figure 4.** Mo 3d SPEM maps within the IDE spacing of (a) ML-$MoS_2$ and (b) IJD-$MoS_2$ chemoresistors.

In ML-$MoS_2$, the IDE spacing appears completely flat with uniform intensity, while in the IJD-$MoS_2$, the contrast variations reflect the typical $MoS_2$ morphology defined by IJD growth as observed in the SEM images in Figure 1e,f. The IDE spacing appears to be different from the nominal one consistent with the SEM images shown before: in the case of ML-$MoS_2$ it is of ∼230 µm instead of 300 µm while in the IJD-$MoS_2$ chemoresistor it is of ∼50 µm instead of 75 µm. These differences are attributed to Ag electrode migration occurring after the screen-printing process, as well as, in the case of IJD-$MoS_2$, to the relatively thick deposited layer, which effectively reduces the apparent IDE spacing by smoothing surface features.

High-resolution XPS spectra of the Mo 3d and S 2s core levels were recorded with the synchrotron beam spot focused on a representative area within the IDE spacing with a diameter of 75 µm. Figure 5 shows the XPS spectra before, during and after $NO_2$ dosing. The spectra recorded during $NO_2$ dosing correspond to the saturation regime, i.e., the gas had interacted with the surface to reach a steady state (>20 min), while the spectra after dosing were acquired after reaching the initial base pressure ($10^{-9}$ mbar). In the case of the ML-$MoS_2$ chemoresistor (Figure 5a), the $Mo^{IV}$ $3d_{5/2}$ peak before $NO_2$ dosing is located at 230.2 eV and shows a rigid shift of about 0.2 eV toward higher binding energies (BEs) during $NO_2$ exposure. The calculated Mo 3d BE shifts, evaluated for a $NO_2$ molecule adsorbed in close proximity to the $MoS_2$ surface (Figure 5d) and referenced to the clean surface configuration (Figure 5e), exhibit a comparable shift toward higher BEs (ΔBE ≈ 0.1 eV), in agreement with the one observed experimentally. This behavior is further supported by spatially resolved BE maps, which reveal a predominant shift of the Mo 3d binding energy toward higher values across the entire IDE spacing under $NO_2$ exposure and applied bias (see Figure S8a,b, Supporting Information). After dosing, the $Mo^{IV}$ $3d_{5/2}$ peak returns to its original position.

The main $Mo^{IV}$ component of the Mo $3d_{5/2}$ peak in IJD-$MoS_2$ (Figure 5b) is centered at 229.5 eV before exposure

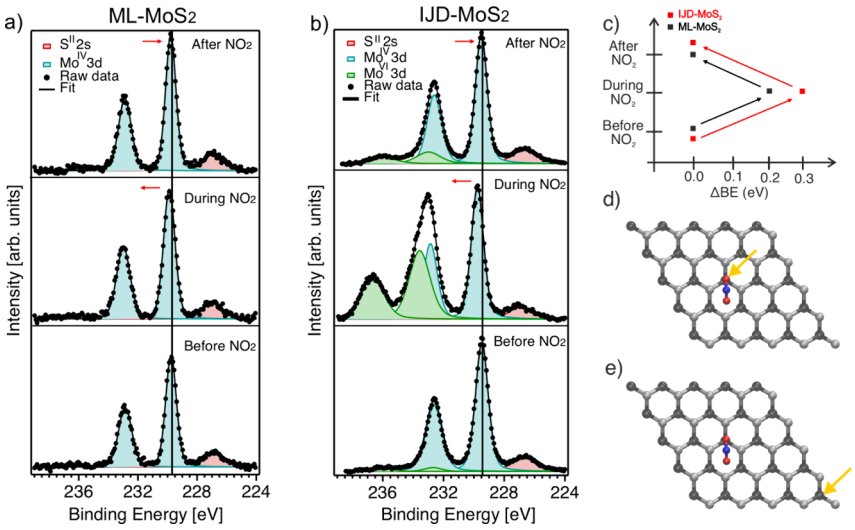


**Figure 5.** Mo 3d and S 2s core level XPS spectra of (a) ML-$MoS_2$ and (b) IJD-$MoS_2$ chemoresistors. (c) Visualization of the Mo 3d BE shifts before, during, and after $NO_2$ dosing for both chemoresistors. (d, e) Mo atoms chosen for the DFT calculation of BE shifts.



https://doi.org/10.1021/acsami.6c04862
ACS Appl. Mater. Interfaces 2026, 18, 41889−41902

Downloaded from pubs.acs.org/aamick/article-pdf/18/30/41889/65852670/am-2026-04862n.pdf by POLITECNICO DI TORINO user on 22 October 2026

and reversibly shifts by ~0.3 eV towards higher BEs upon $NO_2$ dosing, consistent with the BE maps (Figure S8c,d, Supporting Information). In addition, unlike ML-$MoS_2$, a new feature appears on the higher BE side at 233.3 eV, attributable to the formation of $Mo^{VI}$ species, which mainly disappears after dosing.

In Figure 6, the S 2p core level spectra of the ML-$MoS_2$ and IJD-$MoS_2$ are shown, measured before, during, and after $NO_2$ exposure. In the case of the ML-$MoS_2$ chemoresistor (Figure 6a), the S $2p_{3/2}$ peak before $NO_2$ exposure is positioned at 163.1 eV. During $NO_2$ exposure, the spectrum undergoes a rigid shift of about 0.2 eV toward higher BEs, identical to the same shift observed in the Mo 3d core level. Consistently, the calculated S 2p core level shift ($\Delta BE \approx 0.1$ eV) with $NO_2$ in proximity to the $MoS_2$ surface (Figure 6d) compared to the clean configuration (Figure 6e) is in line with the experimentally detected shift toward higher BEs; remarkably, the computed BE variation is essentially the same for Mo 3d and S 2p, in full agreement with the comparable shifts observed experimentally. In addition, the BE maps further corroborate the shift of the S 2p core level toward higher BE across the IDE region during $NO_2$ exposure (Figure S9a,b, Supporting Information).

For the IJD-$MoS_2$ chemoresistor (Figure 6b), the S $2p_{3/2}$ component is located at 162.3 eV before $NO_2$ dosing, in good agreement with the expected BE peak position reported in literature.[55] Upon $NO_2$ injection, a rigid shift of about 0.3 eV toward higher binding energies is observed, consistent with the S 2p BE maps (Figure S9c,d, Supporting Information) and the shift detected in the Mo 3d core level (Figure 5b). Different to the Mo 3d core level of IJD-$MoS_2$, no new components or additional features appear.

After stopping the $NO_2$ injection and pumping down to the base chamber pressure, all the rigid shifts present in the Mo 3d and S 2p core levels during $NO_2$ dosing disappear. Only a small reminiscence of the $Mo^{VI}$ component remains in the IJD-$MoS_2$ chemoresistor.

## ■ DISCUSSION

The comparison between ML-$MoS_2$ and IJD-$MoS_2$ underlines how morphology and thickness of the active material control both the macroscopic sensing performance and the microscopic interaction with $NO_2$. The ML-$MoS_2$ device (Figure 1a−d) features an atomically thin and continuous layer bridging the Ag IDE spacing, with a very smooth surface reflecting the atomically thin nature of ML-$MoS_2$ with only some crater like defects left by the exfoliation process. In contrast, the IJD-$MoS_2$ chemoresistor (Figure 1e−h) displays a rough, three-dimensional morphology with nanometer-sized clusters, and adjacent micro-plates protruding from the surface. This morphology is in line with other nanostructured $MoS_2$ films, in which roughness, edge density and defect concentration substantially increase the number of adsorption sites available for oxidizing gases such as $NO_2$.[23,56] In particular, sulfur vacancies and under-coordinated edge-like Mo atoms are expected to play a major role in the interaction with $NO_2$. Previous theoretical and experimental studies have shown that these defective sites enhance the adsorption strength and promote stronger local electronic perturbations compared to pristine basal-plane $MoS_2$.[23,24,29−31] In the present work, the larger core-level shifts observed for IJD-$MoS_2$, together with the transient $Mo^{VI}$ contribution appearing only during $NO_2$ exposure, are consistent with a higher density of such reactive defect sites. At the same time, the reversibility of both the rigid BE shifts and the $Mo^{VI}$ component after evacuation indicates that these interactions remain weak and dynamic rather than leading to stable oxidation or permanent chemisorption.

Despite its significantly rougher surface and potentially higher adsorption site density, the IJD-$MoS_2$ chemoresistor exhibits a resistance modulation more than an order of magnitude smaller than that of ML-$MoS_2$ at identical $NO_2$ concentrations. This highlights the critical role of thickness: in the $MoS_2$ monolayer, the entire conduction channel is directly involved in surface interactions, whereas in thicker films only a superficial layer contributes, with the bulk acting as a screening conduction reservoir.[57]

The incomplete recovery in $N_2$ observed in Figure 2 for both chemoresistors is also in agreement with previous $NO_2$−$MoS_2$ studies, where room-temperature desorption under inert atmosphere is slow and often requires active recovery strategies such as UV illumination or mild heating to restore the baseline.[57]

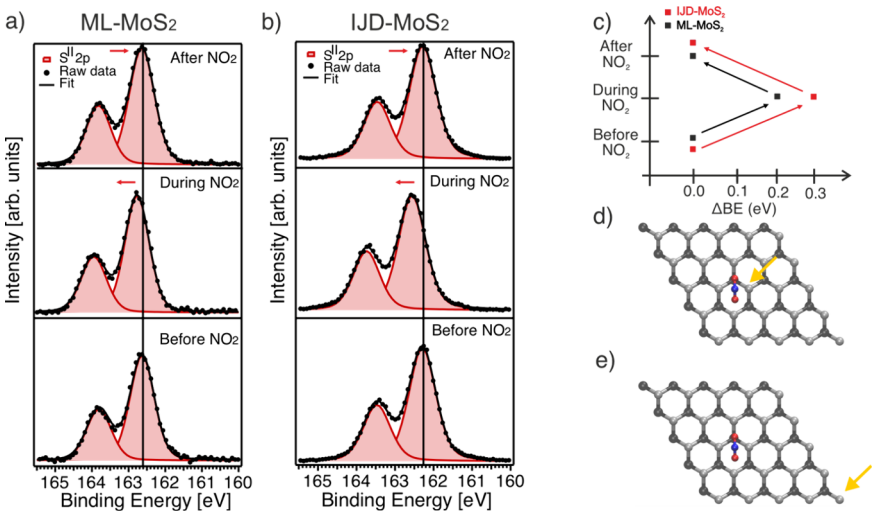


**Figure 6.** S 2p core level XPS spectra of (a) ML-$MoS_2$ and (b) IJD-$MoS_2$ chemoresistors. (c) Schematic showing S 2p core level shifts before, during, and after $NO_2$ dosing of both chemoresistors. (d, e) S atoms chosen for the DFT calculation of BE shifts.



https://doi.org/10.1021/acsami.6c04862
ACS Appl. Mater. Interfaces 2026, 18, 41889−41902

Downloaded from pubs.acs.org/aamick/article-pdf/18/30/41889/65852670/am-2026-04862n.pdf by POLITECNICO DI TORINO user on 22 October 2026

In UHV, the $NO_2$ pulses induce a reproducible increase in resistance in both ML-$MoS_2$ (Figure 3a) and IJD-$MoS_2$ (Figure 3b). The fact that the resistance increases match the behavior in $N_2$ atmosphere, allows for reliable *in operando* XPS/SPEM data acquisition with correlation between chemical reactivity and electrical response. At the same time, the much faster and nearly complete recovery in UHV compared to $N_2$ confirms that the adsorbed $NO_2$ can desorb efficiently once the background atmosphere no longer hinders their removal, pointing towards a non-covalent, weakly bound interaction, as also shown in our previous work on carbon nanotube-based ammonia sensing.[6]

In a previous study, Jensen et al. employed *in operando* SPEM to investigate $NO_x$ adsorption on monolayer $MoS_2$ field-effect transistor (FET) devices on hBN. In that work, $NO_x$ exposure led to Mo 3d core-level shifts toward lower BE, while corresponding S 2p shifts were not reported.[36] This contrasts with the present study, where exposure to $NO_2$ produces shifts of both the Mo 3d and S 2p core levels toward higher BE in both $MoS_2$ samples (IJD and ML). Key experimental differences between the two studies include device architecture (FET with Ti/Au electrodes on hBN versus two-terminal chemoresistors with Ag IDEs on $SiO_2$), gas composition ($NO_x$ mixture vs pure $NO_2$), and different electrostatic boundary conditions. It is important to identify which of these factors are most likely responsible for the different behavior. In our view, the key differences arise not only from the FET configuration, as opposed to the gate-free chemoresistor geometry employed in the present study, but also from the choice and spatial uniformity of the sampled region (e.g., near the electrodes versus within the active channel) and from the gas composition. In addition to the fact that electrostatic gating can modulate the carrier density and induce band bending, ref 36 reports a pronounced spatial heterogeneity of the core-level binding energy particularly in the vicinity of one FET contact. This heterogeneity prevents a general assessment of the behavior across the entire channel and complicates direct comparison with our spatially averaged measurements. Compared with the present study, the interpretation of Jensen et al. is further limited by the absence of corresponding S 2p spectra. Reporting only the Mo 3d core level does not allow one to distinguish a genuine electrostatic shift from changes in the local chemical environment of Mo. In addition, Jensen et al. performed their measurements under a $NO_x$ atmosphere, whereas our experiments were carried out under pure $NO_2$. Because $NO_x$ contains both electron-accepting $NO_2$ and NO, the latter acting as a weak electron donor, the net electrostatic shift in their measurements is not necessarily expected to have the same direction as that observed under pure $NO_2$ exposure. Substrate (hBN vs $SiO_2$) and contact metallurgy, by contrast, are expected to modulate the magnitude and recovery of the response rather than to invert its sign. Importantly, the higher-BE shift reported here is observed reproducibly in two samples with markedly different substrate coupling, morphologies and defect densities (atomically flat ML-$MoS_2$ and rough, defect-rich IJD-$MoS_2$, both on $SiO_2$), which argues that it reflects an intrinsic feature of the $NO_2$−$MoS_2$ interaction probed in a gate-free geometry rather than an artifact of a particular substrate or device. Shifts towards lower BEs are commonly interpreted as electrostatic shifts analogous to upward band bending, consistent with electron transfer from $MoS_2$ to the electron-accepting $NO_2$ molecules and the associated depletion of electrons in the near-surface region. Within this framework, the charge-transfer-induced modifications of the surface electrostatic potential shift all electronic levels uniformly relative to the Fermi level.[58]

By contrast, both ML-$MoS_2$ and IJD-$MoS_2$ chemoresistors investigated here exhibit core-level shifts toward higher BE during $NO_2$ exposure, which are fully reversible (dynamic) once $NO_2$ is removed, as shown in Figures 5 and 6. This opposite trend with respect to previous reports,[36] together with the observed reversibility, points to a different underlying interaction mechanism. At the microscopic level, local charge redistribution and partial (fractional) charge transfer are closely related: any rearrangement of electron density at the adsorption site necessarily involves a fractional redistribution of charge between $NO_2$ and the neighboring Mo and S atoms. The key point is that charge transfer at the interface to the electron-acceptor $NO_2$ would induce an upward band bending, with a corresponding shift of the core levels towards lower BEs. This is contrary to what we observe, namely a shift towards higher BE of both the molybdenum and sulfur core levels. Moreover, this shift is of the same amount for both core levels, which cannot be explained in terms of charge transfer towards the electron-acceptor molecules. Instead, we interpret it in terms of a weaker interaction between the molecules and $MoS_2$, involving a local charge distortion/redistribution due to electronic cloud repulsion between the $NO_2$ and $MoS_2$ valence orbitals, rather than a charge donation. In this respect, the charge reorganization (orbital deformation) at the interface likely causes a reduction of the screening of the valence electrons on the core holes of both Mo and S, thereby increasing the corresponding core-level BEs (i.e., a final-state effect in the photoemission process, whereas a charge transfer would be interpreted as an initial-state effect). Notably, when the $NO_2$ dosing is stopped, the process is completely reversible, i.e., the BEs of the core levels recover to their original values, which is a signature of a weak interaction between the molecules and $MoS_2$. A charge donation between the molecules and $MoS_2$ would make the interaction (bonding) stronger, so that some energy would be required to recover the uncovered $MoS_2$; in our case, the molecules naturally desorb once the molecular dosing is interrupted, suggesting that only a weak interaction is present. These charge redistributions reduce the electronic screening and enhance the effective Coulomb attraction between nuclei and the core electrons, leading to higher BE shifts in the XPS spectra. As illustrated in Figure 7 and from the additional partial charge analysis on defective $MoS_2$ in Figure S6 (Supporting Information), adsorbed $NO_2$ molecules locally and dynamically polarize the electron density of the topmost layer of $MoS_2$, redistributing the valence charge around the adsorption site without electronic charge donation towards $NO_2$. The corresponding DFT charge-density difference maps reveal a redistribution of electronic density localized mainly in the top Mo−S layer and around the adsorbed $NO_2$ molecule, supporting the interpretation of a modified local electronic screening responsible for the observed core-level shifts. This charge rearrangement reduces the electronic screening of the Mo and S nuclei, causing the corresponding core levels to appear more tightly bound, leading to the observed shift to higher BEs in the XPS spectra. The DFT-calculated core-level BE shifts (∼0.1 eV) are quantitatively smaller than the experimentally observed values (∼0.2 eV for ML-$MoS_2$ and ∼0.3 eV for IJD-$MoS_2$), but consistent in sign and trend. This quantitative discrepancy is expected and arises from the idealized nature of the theoretical model. The DFT calculations assume a pristine, free-standing monolayer with a single adsorbed $NO_2$ molecule at

Downloaded from pubs.acs.org/aamick/article-pdf/18/30/41889/65852670/am-2026-04862n.pdf by POLITECNICO DI TORINO user on 22 October 2026



https://doi.org/10.1021/acsami.6c04862
ACS Appl. Mater. Interfaces 2026, 18, 41889−41902

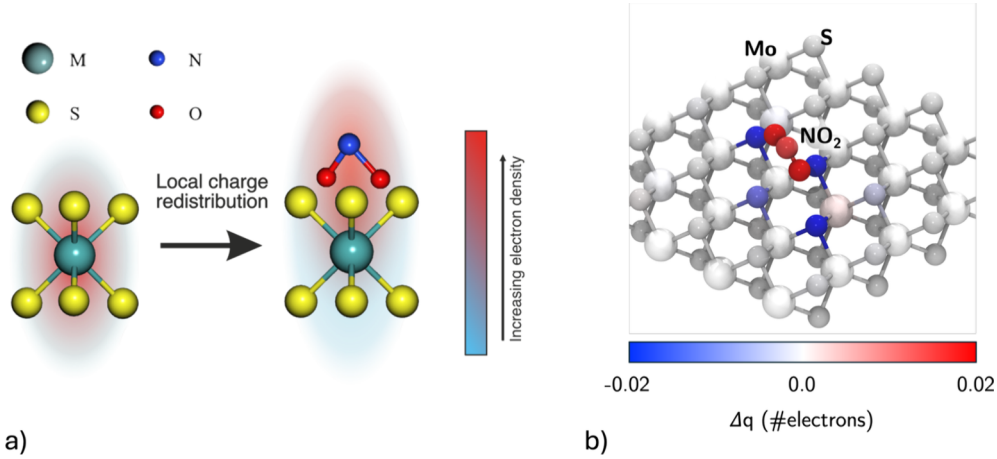


**Figure 7.** (a) Schematic of the topmost layers of $MoS_2$−$NO_2$ interaction leading to reversible (dynamic) local charge redistribution; (b) charge redistribution induced by $NO_2$ adsorption on pristine ML-$MoS_2$ from DFT calculations. The color map shows the change in the number of electrons per atom between the isolated systems and the adsorbed configuration.

low coverage, whereas the experimental measurements were performed under saturation conditions, where the cumulative perturbation from a dense adsorbate layer is expected to produce larger shifts than a single-molecule model. Substrate interactions and applied bias are additional sources of quantitative deviation. In addition, the core-level energies were computed within a Slater transition-state (half-core-hole) ΔSCF scheme, which is reliable for trends but may underestimate the BE shift when final-state screening depends strongly on the local environment. Nevertheless, the agreement in the direction and relative magnitude of the shifts between theory and experiment provides support for the proposed dynamic charge redistribution mechanism.

*In operando* XPS analysis of the Mo 3d and S 2p regions (Figures 5 and 6) shows that $NO_2$ induces fully reversible electronic modifications in both ML-$MoS_2$ and IJD-$MoS_2$, in agreement with the weak interaction mechanism proposed here. ML-$MoS_2$ exhibits a rigid shift of approximately 0.2 eV toward higher binding energies upon $NO_2$ exposure (Figures 5a and 6a), with complete recovery after evacuation. IJD-$MoS_2$ shows slightly larger shifts (∼0.3 eV; Figures 5b and 6b) and a transient $Mo^{VI}$ contribution that disappears after $NO_2$ removal. The absence of persistent spectral changes in either system rules out stable chemisorption and supports a reversible redistribution of charges at the topmost surface layer. This is consistent with theoretical work showing that $NO_x$ can interact with $MoS_2$ via charge redistribution while remaining in a physisorbed or weakly chemisorbed van-der-Waals regime, especially at defect or edge sites.[29]

The consequences of this mechanism for electronic transport can be understood through the relation between resistance and conductivity $R = \frac{L}{\sigma A}$ where $L$ is the channel length, $A$ is the effective conduction cross-section and σ is the conductivity that can be expressed as follows:

$$\sigma = n e \mu$$

where $n$ is the electron carrier concentration, $e$ is the charge of the electron and μ is the mobility. In the present case, the reversible $NO_2$-induced resistance increase is most plausibly interpreted as arising from a reduction in carrier mobility rather than from a substantial depletion of free carriers, although the two contributions cannot be fully disentangled from the present dataset alone. The local polarization of the electronic density induced by adsorbed $NO_2$ molecules modifies the electrostatic potential landscape at the $MoS_2$ surface, creating spatially localized perturbations that act as additional scattering centers for charge carriers traversing the conduction channel. This enhanced scattering reduces the carrier mobility μ and therefore increases the resistance as observed in Figures 2 and 3. The complete reversibility of both the electrical response and the XPS core-level shifts after $NO_2$ removal is consistent with such a dynamic, predominantly mobility-driven mechanism. A direct and quantitative separation of the mobility and carrier-density contributions would require complementary Hall-effect or gated field-effect transport measurements. These are not accessible in the present two-terminal, gate-free chemoresistor geometry, which was specifically designed for *in operando* XPS/SPEM under UHV $NO_2$ dosing; we therefore present the mobility-dominated picture as a likely interpretation consistent with all available evidence. In ML-$MoS_2$, the entire conduction channel coincides with the exposed surface, therefore any local reduction in $n$ and μ directly affects the only available current path and results in a pronounced resistance modulation. In IJD-$MoS_2$, by contrast, as the $NO_2$−$MoS_2$ interaction is confined to a limited surface region, and deeper layers of the nm-thick film remain largely unaffected and provide alternative conduction paths. This effect explains why the IJD-$MoS_2$ thin film exhibits larger core-level shifts (within the topmost ∼5 nm probed by XPS) than the monolayer, while showing a much smaller net change in resistance.

The transient $Mo^{VI}$ component observed in the Mo 3d core level region of IJD-$MoS_2$ during $NO_2$ dosing (Figure 5b) can be understood in terms of beam-induced photodissociation of $NO_2$ under synchrotron irradiation and interaction with the highly defect-rich IJD-$MoS_2$ surface. High-energy photons can promote dissociation channels such as $NO_2 \rightarrow NO^* + O^*$, similar $NO_2$-induced, photon-assisted oxidation phenomena have been reported for other 2D materials, for example, reversible oxidation of graphene by $NO_2$ under X-ray or UV illumination.[59−62] In the IJD-$MoS_2$ film, the atomic oxygen and NO fragments produced during photodissociation can temporarily occupy sulfur vacancies—expected to be more


https://doi.org/10.1021/acsami.6c04862
ACS Appl. Mater. Interfaces 2026, 18, 41889−41902

Downloaded from pubs.acs.org/aamick/article-pdf/18/30/41889/65852670/am-2026-04862n.pdf by POLITECNICO DI TORINO user on 22 October 2026

abundant due to the IJD growth and annealing conditions—or bind weakly to under-coordinated Mo atoms at the surface, forming transient Mo−O bonds. This process is depicted in Figure 8, where $NO_2$ photodissociation in the X-ray beam leads to a reversible conversion of a fraction of $Mo^{IV}$ to $Mo^{VI}$. The fact that the $Mo^{VI}$ signal mainly disappears after pumping, and that the S 2p spectra (Figure 6b) show no permanent new components, confirms that no stable $Mo^{VI}$ oxidation states were formed, consistent with weakly bound transient states rather than true chemisorbed species. It is worth noting that this transient $Mo^{VI}$ component is specific to the synchrotron measurement environment, where high-energy, high-flux photons promote $NO_2$ photodissociation pathways that are absent under conventional dark, room-temperature sensing conditions. The fully reversible nature of this component upon gas removal, together with the absence of new S 2p features, confirms that no stable molybdenum oxide phases accumulate, which is encouraging for long-term sensor cycling stability.

Overall, the present study allows us to position our results within the broader landscape of $MoS_2$-based $NO_2$ sensors. Chemically exfoliated and defect-engineered $MoS_2$ systems have been shown to achieve $NO_2$ detection limits down to tens of ppb by exploiting high surface-to-volume ratio and engineered vacancy densities.[23,57] Our ML-$MoS_2$ device conforms to this "ideal 2D" paradigm: despite its limited absolute surface area, the coupling between surface charge redistribution and conduction is maximized. The IJD-$MoS_2$ sensor, instead, represents a scalable nanostructured $MoS_2$ thin-film architecture in which the rough, edge- and defect-rich morphology promotes a larger total charge exchange with $NO_2$ but the bulk-like conduction strongly attenuates the electrical signature of this interaction. The fact that both systems display local charge redistribution and reversible interactions, yet with very different macroscopic responses, illustrates how morphology, defect distribution and conduction volume must be coengineered to translate favorable surface chemistry into high-performance $NO_2$ detection in $MoS_2$-based chemoresistive devices.

## ■ CONCLUSIONS

In this work, we elucidated the microscopic origin of $NO_2$ sensing in $MoS_2$ chemoresistors by directly correlating macroscopic electrical responses with local electronic-structure changes under realistic operating conditions. For this purpose, we combined controlled gas sensing with *in operando* micro-focused XPS and SPEM analysis supported by DFT calculations to investigate atomically thin $MoS_2$ monolayer and nanostructured, defect-rich $MoS_2$ thin films, i.e., two extreme cases concerning morphology, defectivity, and thickness (2D vs 3D).

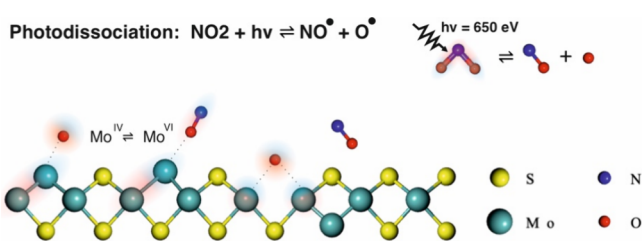


**Figure 8.** Schematic showing the photodissociation process of $NO_2$ and the subsequent interaction with the IJD-$MoS_2$ chemoresistor transiently changing the oxidation state of some Mo atoms from IV to VI.

Both systems exhibit a reproducible increase in resistance upon $NO_2$ exposure, accompanied by rigid shifts of the Mo 3d and S 2p core levels towards higher binding energies. The $NO_2$−$MoS_2$ surface interaction is reversible, with no evidence of permanent chemical modification. This indicates that $NO_2$ detection in $MoS_2$ does not primarily arise from net charge-transfer doping, which would be expected to produce band bending indirectly observable in XPS. Instead, our results are best explained by a mechanism dominated by dynamic, local charge redistribution at the $MoS_2/NO_2$ interface. Microscopically, this involves a reduction of the photoemission final state screening of the core levels caused by the local reorganization of valence charge through Coulomb repulsion, without any net doping of the channel. This interpretation is consistent with the shifts of the core levels towards higher binding energy observed in XPS and with the resulting sensing response.

In defect-rich IJD-$MoS_2$ thin films, we additionally observe a transient $Mo^{VI}$ component during $NO_2$ exposure, which we attribute to weak and reversible Mo−O interactions at defect sites, likely promoted by photon-assisted $NO_2$ dissociation under synchrotron irradiation. The disappearance of this component after gas removal confirms the absence of stable oxidation and reinforces the picture of weak, reversible interactions dominating the sensing process.

In the $MoS_2$ monolayer, where the entire conduction channel coincides with the surface, local charge redistribution directly translates into large resistance modulations. In thicker nanostructured films, surface-confined electronic perturbations are effectively screened by bulk-like conduction pathways, leading to smaller macroscopic responses despite stronger local chemical interactions.

Our results provide a unified and experimentally grounded framework for understanding $NO_2$ sensing in $MoS_2$ across different morphologies, defectivities and thicknesses. Beyond resolving long-standing ambiguities about charge transfer vs electrostatic effects, this study establishes dynamic charge redistribution as a key principle for $MoS_2$-based gas sensors. Furthermore, our study demonstrates that SPEM/XPS under $NO_2$ dosing can be used to probe transient chemical species that are a hallmark for the heterogeneity of the surface. These insights bridge ideal 2D model systems with scalable 3D thin-film architectures and offer clear guidelines for engineering high-performance, low-power $NO_2$ sensors based on $MoS_2$.

## ■ ASSOCIATED CONTENT

### Data Availability Statement

The authors declare that all data supporting the findings of this study are available within the paper; source data for the figures in this study are available from the authors upon request.

### Supporting Information

The Supporting Information is available free of charge at https://pubs.acs.org/doi/10.1021/acsami.6c04862.

Figure S1: Electrical response of the IJD-$MoS_2$ chemoresistor during exposure to $NH_3$, $NO_2$, and $CO_2$; Figure S2: Sequential scans of Mo 3d and S 2s core level XPS spectra of ML-$MoS_2$ and IJD-$MoS_2$ chemoresistors; Figure S3: Sequential scans of S 2p core level XPS spectra of ML-$MoS_2$ and IJD-$MoS_2$ chemoresistors; Figure S4: N 1s XPS core level of ML-$MoS_2$ and IJD-$MoS_2$; Figure S5: Cross-sectional TEM view

Downloaded from pubs.acs.org/aamick/article-pdf/18/30/41889/65852670/am-2026-04862n.pdf by POLITECNICO DI TORINO user on 22 October 2026


https://doi.org/10.1021/acsami.6c04862
ACS Appl. Mater. Interfaces 2026, 18, 41889−41902

of the $MoS_2$ plate like structures protruding from the IJD-$MoS_2$ surface; Figure S6: Charge redistribution plot in the case of $NO_2$ interacting with a $MoS_2$ monolayer with a S vacancy; Figure S7: SPEM maps of ML-$MoS_2$ and IJD-$MoS_2$ taken in the Mo 3d core level region before and during $NO_2$ injection; Figure S8: SPEM maps of ML-$MoS_2$ and IJD-$MoS_2$ taken in the S 2p core level region before and during $NO_2$ injection (DOCX)

## ■ AUTHOR INFORMATION


### Corresponding Authors

**Cristian Tomasi Cebotari** – *CNR-IMEM Institute of Materials for Electronics and Magnetism, Trento unit c/o Fondazione Bruno Kessler, Via alla Cascata 56/C, Trento 38123, Italy; Department of Chemistry, Life Science and Environmental Sustainability, University of Parma, Parco Area delle Scienze 17/A, Parma 43124, Italy;* Email: cristian.tomasicebotari@unipr.it

**Marco Vittorio Nardi** – *CNR-IMEM Institute of Materials for Electronics and Magnetism, Trento unit c/o Fondazione Bruno Kessler, Via alla Cascata 56/C, Trento 38123, Italy;* orcid.org/0000-0002-7279-3543; Email: marcovittorio.nardi@cnr.it

**Melanie Timpel** – *CNR-IMEM Institute of Materials for Electronics and Magnetism, Trento unit c/o Fondazione Bruno Kessler, Via alla Cascata 56/C, Trento 38123, Italy;* orcid.org/0000-0002-7432-3086; Email: melaniekristina.timpel@cnr.it

### Authors

**Christos Gatsios** – *CNR-IMEM Institute of Materials for Electronics and Magnetism, Trento unit c/o Fondazione Bruno Kessler, Via alla Cascata 56/C, Trento 38123, Italy*

**Antonello Mascia** – *Department of Electrical and Electronics Engineering, University of Cagliari, Piazza D'Armi, Cagliari 09123, Italy;* orcid.org/0000-0002-4185-7225

**Steffen Rühl** – *Department of Physics, Department of Chemistry & Center for the Science of Materials Berlin, Humboldt-Universität zu Berlin, Zum Großen Windkanal 2, Berlin 12489, Germany*

**Sahira Vasquez** – *Sensing Technologies Laboratory (STL), Faculty of Engineering, Free University of Bozen-Bolzano, via Bruno Buozzi 1, Bolzano 39100, Italy*

**Andrea Pedrielli** – *Sensors and Devices Center, Fondazione Bruno Kessler (FBK), Via Sommarive 18, Trento 38123, Italy*

**Matteo Amati** – *Elettra-Sincrotrone Trieste S.C.p.A, Strada Statale 14 - km 163.5 in AREA Science Park, Basovizza, Trieste 34149, Italy*

**Zygmunt Milosz** – *Elettra-Sincrotrone Trieste S.C.p.A, Strada Statale 14 - km 163.5 in AREA Science Park, Basovizza, Trieste 34149, Italy;* orcid.org/0000-0002-4938-9331

**Luca Gregoratti** – *Elettra-Sincrotrone Trieste S.C.p.A, Strada Statale 14 - km 163.5 in AREA Science Park, Basovizza, Trieste 34149, Italy;* orcid.org/0000-0002-1277-6733

**Francesca Risplendi** – *Department of Applied Science and Technology, Politecnico di Torino, Corso Duca degli Abruzzi 24, Torino 10129, Italy*

**Michele Re Fiorentin** – *Department of Applied Science and Technology, Politecnico di Torino, Corso Duca degli Abruzzi 24, Torino 10129, Italy*

**Francesca Rossi** – *CNR-IMEM Institute of Materials for Electronics and Magnetism, Parco Area delle Scienze 37/A, Parma 43124, Italy;* orcid.org/0000-0003-1773-2542

**Lucia Nasi** – *CNR-IMEM Institute of Materials for Electronics and Magnetism, Parco Area delle Scienze 37/A, Parma 43124, Italy*

**Giovanni Ligorio** – *Department of Physics, Department of Chemistry & Center for the Science of Materials Berlin, Humboldt-Universität zu Berlin, Zum Großen Windkanal 2, Berlin 12489, Germany;* orcid.org/0000-0001-9277-6903

**Emil J.W. List-Kratochvil** – *Department of Physics, Department of Chemistry & Center for the Science of Materials Berlin, Humboldt-Universität zu Berlin, Zum Großen Windkanal 2, Berlin 12489, Germany; Helmholtz−Zentrum Berlin für Materialien und Energie, Hahn−Meitner−Platz 1, Berlin 14109, Germany;* orcid.org/0000-0001-9206-800X

**Roberto Verucchi** – *CNR-IMEM Institute of Materials for Electronics and Magnetism, Trento unit c/o Fondazione Bruno Kessler, Via alla Cascata 56/C, Trento 38123, Italy;* orcid.org/0000-0001-6850-3980

**Luca Pasquali** – *Dipartimento di Ingegneria "Enzo Ferrari", Università degli studi di Modena e Reggio Emilia, Via Università, 4, Modena 41121, Italy; CNR - Istituto Officina dei Materiali (IOM), Strada Statale 14, Km. 163.5 in AREA Science Park, Basovizza, Trieste 34149, Italy; Department of Physics, University of Johannesburg, Auckland Park 2006, South Africa;* orcid.org/0000-0003-0399-7240

**Luisa Petti** – *Sensing Technologies Laboratory (STL), Faculty of Engineering, Free University of Bozen-Bolzano, via Bruno Buozzi 1, Bolzano 39100, Italy;* orcid.org/0000-0003-0264-7185

**Piero Cosseddu** – *Department of Electrical and Electronics Engineering, University of Cagliari, Piazza D'Armi, Cagliari 09123, Italy*

Complete contact information is available at: https://pubs.acs.org/doi/10.1021/acsami.6c04862


### Author Contributions

C.T.C.: formal analysis, methodology, investigation, visualization, data curation, writing−original draft, and writing−review and editing; S.R.: methodology and writing−review and editing; G.L.: methodology and writing−review and editing; C.G.: methodology, investigation, and writing−review and editing; S.V.: methodology, formal analysis, and writing−review and editing; A.M.: formal analysis, investigation, data curation, and writing−review and editing; A.P.: formal analysis, investigation, data curation, and writing−review and editing; M.A.: investigation and data curation; Z.M.: investigation; L.G.: investigation; F. Risplendi: investigation, data curation, and writing−review and editing; M.R.F.: investigation, data curation, and writing−review and editing; F. Rossi: investigation, data curation, and writing - review and editing; L.N.: formal analysis, investigation, data curation, and writing−review and editing; E.L.-K.: resources, writing−review and editing, and supervision; P.C.: resources and writing−review and editing funding acquisition; Luisa P.: resources and writing−review and editing; Luca P.: writing−review and editing funding acquisition; R.V.: resources and funding acquisition; M.V.N.: conceptualization, methodology, formal analysis, investigation,

Downloaded from pubs.acs.org/aamick/article-pdf/18/30/41889/65852670/am-2026-04862n.pdf by POLITECNICO DI TORINO user on 22 October 2026

visualization, resources, writing−review and editing, supervision, project administration, and funding acquisition; M.T.: conceptualization, methodology, formal analysis, investigation, visualization, resources, writing−review and editing, supervision, project administration, and funding acquisition.

### Notes

The authors declare no competing financial interest.

## ■ ACKNOWLEDGMENTS

The authors would like to thank L. Lorenzelli for providing the $SiO_2$ thermal oxide substrates. C.T.C., M.T., and F. Risplendi acknowledge financial support of the project PRIN 2022 Project '2D-EMMA' (Project n. 202289PMBP) in the frame of Next Generation EU. C.C. and M.V.N. acknowledge financial support of the project PRIN 2022 Project 'PETRA' (Project n. 2022T7ZSEK) in the frame of Next Generation EU. R.V. is part of the innovation Ecosystem of the project "RAISE - Robotics and AI for Socio-economic Empowerment " (ECS00000035) and has been supported by the European Union - NextGenerationEU, the Ministry of University and Research (MUR), National Recovery and Resilience Plan (NRRP), Mission 4, Component 2, Investment 1.5, CUP: ECS00000035. Funded by the European Union - NextGenerationEU, Mission 4, Component 1, CUP D53D23016540001. This work was carried out in the framework of the Joint Lab GEN_FAB. M.R.F. and F. Risplendi acknowledge CINECA for the high-performance computing resources provided under the ISCRA initiative.

## ■ REFERENCES

(1) Hou, H. L.; Anichini, C.; Samorì, P.; Criado, A.; Prato, M. 2D Van Der Waals Heterostructures for Chemical Sensing. *Adv. Funct. Mater.* **2022**, *32* (49), No. 2207065.

(2) Ottaviano, L.; Mastrippolito, D. The Future Ahead Gas Sensing with Two-Dimensional Materials. *Appl. Phys. Lett.* **2023**, *123* (5), No. 050502.

(3) Donarelli, M.; Ottaviano, L. 2D Materials for Gas Sensing Applications: A Review on Graphene Oxide, $MoS_2$, $WS_2$ and Phosphorene. *Sensors* **2018**, *18* (11), 3638.

(4) Wang, C.; Yin, L.; Zhang, L.; Xiang, D.; Gao, R. Metal Oxide Gas Sensors: Sensitivity and Influencing Factors. *Sensors* **2010**, *10* (3), 2088−2106.

(5) Vasquez, S.; Costa Angeli, M. A.; Petrelli, M.; Ahmad, M.; Shkodra, B.; Salonikidou, B.; Sporea, R. A.; Rivadeneyra, A.; Lugli, P.; Petti, L. Comparison of Printing Techniques for the Fabrication of Flexible Carbon Nanotube-Based Ammonia Chemiresistive Gas Sensors. *Flex. Print. Electron.* **2023**, *8* (3), No. 035012.

(6) Gatsios, C.; Mascia, A.; Tomasi Cebotari, C.; Vasquez, S.; Milosz, Z.; Pedrielli, A.; Amati, M.; Gregoratti, L.; Petti, L.; Cosseddu, P.; Pasquali, L.; Timpel, M.; Nardi, M. V. Assessing the Mechanism of $NH_3$ Sensing in Flexible Carbon-Nanotube-Based Chemoresistive Sensors via In Situ Photoemission Spectroscopy. *Adv. Mater. Interfaces* **2026**, *13*, No. e00893.

(7) Luo, K.; Peng, H.; Zhang, B.; Chen, L.; Zhang, P.; Peng, Z.; Fu, X. Advances in Carbon Nanotube-Based Gas Sensors: Exploring the Path to the Future. *Coord. Chem. Rev.* **2024**, *518*, No. 216049.

(8) Lee, Y. H.; Zhang, X. Q.; Zhang, W.; Chang, M. T.; Lin, C.-T.; Chang, K.-D.; Yu, Y. C.; Wang, J. T. W.; Chang, C. S.; Li, L. J.; Lin, T. W. Synthesis of Large-Area $MoS_2$ Atomic Layers with Chemical Vapor Deposition. *Adv. Mater.* **2012**, *24* (17), 2320−2325.

(9) Singh, D. K.; Pant, R. K.; Nanda, K. K.; Krupanidhi, S. B. Pulsed Laser Deposition for Conformal Growth of $MoS_2$ on GaN Nanorods for Highly Efficient Self-Powered Photodetection. *Mater. Adv.* **2022**, *3* (15), 6343−6351.

(10) Tumino, F.; Casari, C. S.; Passoni, M.; Russo, V.; Li Bassi, A. Pulsed Laser Deposition of Single-Layer $MoS_2$ on Au(111): From Nanosized Crystals to Large-Area Films. *Nanoscale Adv.* **2019**, *1* (2), 643−655.

(11) Zhong, W.; Deng, S.; Wang, K.; Li, G.; Li, G.; Chen, R.; Kwok, H. S. Feasible Route for a Large Area Few-Layer $MoS_2$ with Magnetron Sputtering. *Nanomaterials* **2018**, *8* (8), 590.

(12) Hussain, S.; Singh, J.; Vikraman, D.; Singh, A. K.; Iqbal, M. Z.; Khan, M. F.; Kumar, P.; Choi, D. C.; Song, W.; An, K. S.; Eom, J.; Lee, W. G.; Jung, J. Large-Area, Continuous and High Electrical Performances of Bilayer to Few Layers $MoS_2$ Fabricated by RF Sputtering via Post-Deposition Annealing Method. *Sci. Rep.* **2016**, *6*, 30791.

(13) Timpel, M.; Ligorio, G.; Ghiami, A.; Gavioli, L.; Cavaliere, E.; Chiappini, A.; Rossi, F.; Pasquali, L.; Gärisch, F.; List-Kratochvil, E. J. W.; Nozar, P.; Quaranta, A.; Verucchi, R.; Nardi, M. V. 2D-$MoS_2$ Goes 3D: Transferring Optoelectronic Properties of 2D $MoS_2$ to a Large-Area Thin Film. *npj 2D Mater. Appl.* **2021**, *5* (1), 64.

(14) Ghiami, A.; Timpel, M.; Chiappini, A.; Nardi, M. V.; Verucchi, R. Synthesis of $MoS_2$ Thin Film by Ionized Jet Deposition: Role of Substrate and Working Parameters. *Surfaces* **2020**, *3*, 683−693.

(15) George, A. S.; Mutlu, Z.; Ionescu, R.; Wu, R. J.; Jeong, J. S.; Bay, H. H.; Chai, Y.; Mkhoyan, K. A.; Ozkan, M.; Ozkan, C. S. Wafer Scale Synthesis and High Resolution Structural Characterization of Atomically Thin $MoS_2$ Layers. *Adv. Funct. Mater.* **2014**, *24* (47), 7461−7466.

(16) Nardi, M. V.; Timpel, M.; Ligorio, G.; Zorn Morales, N.; Chiappini, A.; Toccoli, T.; Verucchi, R.; Ceccato, R.; Pasquali, L.; List-Kratochvil, E. J. W.; Quaranta, A.; Dirè, S. Versatile and Scalable Strategy to Grow Sol-Gel Derived 2H-$MoS_2$ Thin Films with Superior Electronic Properties: A Memristive Case. *ACS Appl. Mater. Interfaces* **2018**, *10* (40), 34392−34400.

(17) Kumar, R.; Zheng, W.; Liu, X.; Zhang, J.; Kumar, M. $MoS_2$-Based Nanomaterials for Room-Temperature Gas Sensors. *Adv. Mater. Technol.* **2020**, *5* (5), No. 1901062.

(18) Kumar, S.; Betal, A.; Kumar, A.; Chakkar, A. G.; Kumar, P.; Kwoka, M.; Sahu, S.; Kumar, M. Enhancing $NO_2$ Gas Sensing: The Dual Impact of UV and Thermal Activation on Vertically Aligned Nb-$MoS_2$ for Superior Response and Selectivity. *ACS Sens.* **2025**, *10* (3), 2191−2202.

(19) Bhattarai, K.; Lamsal, L.; Gyawali, M.; Neupane, S.; Gautam, S. P.; Bakshi, A.; Yeager, J. Impact of Nitrogen Dioxide ($NO_2$) Pollution on Asthma: The Case of Louisiana State (2005−2020). *Atmosphere* **2024**, *15*, 1472.

(20) Latza, U.; Gerdes, S.; Baur, X. Effects of Nitrogen Dioxide on Human Health: Systematic Review of Experimental and Epidemiological Studies Conducted between 2002 and 2006. *Int. J. Hyg. Environ. Health* **2009**, *212* (3), 271−287.

(21) Huang, S.; Li, H.; Wang, M.; Qian, Y.; Steenland, K.; Caudle, W. M.; Liu, Y.; Sarnat, J.; Papatheodorou, S.; Shi, L. Long-Term Exposure to Nitrogen Dioxide and Mortality: A Systematic Review and Meta-Analysis. *Sci. Total Environ.* **2021**, *776*, No. 145968.

(22) Kim, S.; Park, H.; Choo, S.; Baek, S.; Kwon, Y.; Liu, N.; Yang, J. Y.; Yang, C. W.; Yoo, G.; Kim, S. Active-Matrix Monolithic Gas Sensor Array Based on $MoS_2$ Thin-Film Transistors. *Commun. Mater.* **2020**, *1* (1), 86.

(23) Donarelli, M.; Prezioso, S.; Perrozzi, F.; Bisti, F.; Nardone, M.; Giancaterini, L.; Cantalini, C.; Ottaviano, L. Response to $NO_2$ and Other Gases of Resistive Chemically Exfoliated $MoS_2$-Based Gas Sensors. *Sens. Actuators, B* **2015**, *207*, 602−613.

(24) Kumar, R. R.; Habib, M. R.; Khan, A.; Chen, P. C.; Murugesan, T.; Gupta, S.; Anbalagan, A. K.; Tai, N. H.; Lee, C. H.; Lin, H. N. Sulfur Monovacancies in Liquid-Exfoliated $MoS_2$ Nanosheets for $NO_2$ Gas Sensing. *ACS Appl. Nano Mater.* **2021**, *4* (9), 9459−9470.

(25) Ramaraj, S. G.; Nundy, S.; Zhao, P.; Elamaran, D.; Tahir, A. A.; Hayakawa, Y.; Muruganathan, M.; Mizuta, H.; Kim, S. W. RF Sputtered Nb-Doped $MoS_2$ Thin Film for Effective Detection of $NO_2$ Gas Molecules: Theoretical and Experimental Studies. *ACS Omega* **2022**, *7* (12), 10492−10501.

Downloaded from pubs.acs.org/aamick/article-pdf/18/30/41889/65852670/am-2026-04862n.pdf by POLITECNICO DI TORINO user on 22 October 2026



https://doi.org/10.1021/acsami.6c04862
ACS Appl. Mater. Interfaces 2026, 18, 41889−41902

(26) Zhang, K.; Deng, D. D.; Zheng, B.; Wang, Y.; Perkins, F. K.; Briggs, N. C.; Crespi, V. H.; Robinson, J. A. Tuning Transport and Chemical Sensitivity via Niobium Doping of Synthetic $MoS_2$. *Adv. Mater. Interfaces* **2020**, *7* (18), No. 2000856.
(27) Late, D. J.; Huang, Y. K.; Liu, B.; Acharya, J.; Shirodkar, S. N.; Luo, J.; Yan, A.; Charles, D.; Waghmare, U. V.; Dravid, V. P.; Rao, C. N. R. Sensing Behavior of Atomically Thin-Layered $MoS_2$ Transistors. *ACS Nano* **2013**, *7* (6), 4879−4891.
(28) Kushwaha, A.; Goel, N. Edge Enriched $MoS_2$ Micro Flowered Structure for High Performance $NO_2$ Sensor. *Sens. Actuators, B* **2023**, *393*, No. 134190.
(29) Zhao, S.; Xue, J.; Kang, W. Gas Adsorption on $MoS_2$ Monolayer from First-Principles Calculations. *Chem. Phys. Lett.* **2014**, *595*−*596*, 35−42.
(30) Szary, M. J.; Bąbelek, J. A.; Florjan, D. M. Adsorption and Dissociation of $NO_2$ on $MoS_2$ Doped with P-Block Elements. *Surf. Sci.* **2021**, *712*, No. 121893.
(31) Yue, Q.; Shao, Z.; Chang, S.; Li, J. Adsorption of Gas Molecules on Monolayer $MoS_2$ and Effect of Applied Electric Field. *Nanoscale Res. Lett.* **2013**, *8*, 425.
(32) Bianchi, M. G.; Risplendi, F.; Re Fiorentin, M.; Cicero, G. Addressing the Effects of Gas Adsorption on Monolayers beyond Charge Population Analysis: The Case of $WS_2$. *npj Comput. Mater.* **2024**, *10* (1), 62.
(33) Scardamaglia, M.; Casanova-Cháfer, J.; Temperton, R.; Annanouch, F. E.; Mohammadpour, A.; Malandra, G.; Das, A.; Alagh, A.; Arbouch, I.; Montoisy, L.; Cornil, D.; Cornil, J.; Llobet, E.; Bittencourt, C. Operando Investigation of $WS_2$ Gas Sensors: Simultaneous Ambient Pressure X-Ray Photoelectron Spectroscopy and Electrical Characterization in Unveiling Sensing Mechanisms during Toxic Gas Exposure. *ACS Sens.* **2024**, *9* (8), 4079−4088.
(34) Meng, C.; Das, P.; Shi, X.; Fu, Q.; Müllen, K.; Wu, Z. S. In Situ and Operando Characterizations of 2D Materials in Electrochemical Energy Storage Devices. *Small Sci.* **2021**, *1* (4), No. 2000076.
(35) Amati, M.; Gregoratti, L.; Zeller, P.; Greiner, M.; Scardamaglia, M.; Junker, B.; Ruß, T.; Weimar, U.; Barsan, N.; Favaro, M.; Alharbi, A.; Jensen, I. J. T.; Ali, A.; Belle, B. D. Near Ambient Pressure Photoelectron Spectro-Microscopy: From Gas-Solid Interface to Operando Devices. *J. Phys. D: Appl. Phys.* **2021**, *54* (20), No. 204004.
(36) Jensen, I. J. T.; Ali, A.; Zeller, P.; Amati, M.; Schrade, M.; Vullum, P. E.; Muñiz, M. B.; Bisht, P.; Taniguchi, T.; Watanabe, K.; Mehta, B. R.; Gregoratti, L.; Belle, B. D. Direct Observation of Charge Transfer between $NO_x$ and Monolayer $MoS_2$ by Operando Scanning Photoelectron Microscopy. *ACS Appl. Nano Mater.* **2021**, *4* (4), 3319−3324.
(37) Ji, H.; Zeng, W.; Li, Y. Gas Sensing Mechanisms of Metal Oxide Semiconductors: A Focus Review. *Nanoscale* **2019**, *11* (47), 22664−22684.
(38) Minezaki, T.; Krüger, P.; Annanouch, F. E.; Casanova-Cháfer, J.; Alagh, A.; Villar-Garcia, I. J.; Pérez-Dieste, V.; Llobet, E.; Bittencourt, C. Hydrogen Sensing Mechanism of $WS_2$ Gas Sensors Analyzed with DFT and NAP-XPS. *Sensors* **2023**, *23* (10), 4623.
(39) Müller, J.; Heyl, M.; Schultz, T.; Elsner, K.; Schloz, M.; Rühl, S.; Seiler, H.; Koch, N.; List-Kratochvil, E. J. W.; Koch, C. T. Probing Crystallinity and Grain Structure of 2D Materials and 2D-Like Van Der Waals Heterostructures by Low-Voltage Electron Diffraction. *Phys. Status Solidi A* **2024**, *221* (1), No. 2300148.
(40) Tomasi Cebotari, C.; Gatsios, C.; Pedrielli, A.; Nasi, L.; Rossi, F.; Chiappini, A.; Ceccato, R.; Verucchi, R.; Nardi, M. V.; Timpel, M. Optimizing Crystalline $MoS_2$ Growth on Technologically Relevant Platinum Substrates Using Ionized Jet Deposition: Interface Interactions and Structural Insights. *Surfaces* **2025**, *8*, 38.
(41) Heyl, M.; Burmeister, D.; Schultz, T.; Pallasch, S.; Ligorio, G.; Koch, N.; List-Kratochvil, E. J. W. Thermally Activated Gold-Mediated Transition Metal Dichalcogenide Exfoliation and a Unique Gold-Mediated Transfer. *Phys. Status Solidi RRL* **2020**, *14* (11), No. 2000408.
(42) Nijkoops, A.; Ciocca, M.; Krik, S.; Douaki, A.; Gurusekaran, A.; Vasquez, S.; Petrelli, M.; Angeli, M. A. C.; Petti, L.; Lugli, P. Flexible and Printed Chemiresistive Ammonia Gas Sensors Based on Carbon Nanotube and Conjugated Polymers: A Comparison of Response and Recovery Performance. *IEEE Sens. Lett.* **2023**, *7* (6), No. 2001004.
(43) Amati, M.; Kazemian Abyaneh, M.; Gregoratti, L. Dynamic High Pressure: A Novel Approach toward near Ambient Pressure Photoemission Spectroscopy and Spectromicroscopy. *J. Instrum.* **2013**, *8* (5), No. T05001.
(44) Major, G. H.; Fairley, N.; Sherwood, P. M. A.; Linford, M. R.; Terry, J.; Fernandez, V.; Artyushkova, K. Practical Guide for Curve Fitting in X-Ray Photoelectron Spectroscopy. *J. Vac. Sci. Technol. A* **2020**, *38*, No. 061203.
(45) Grünleitner, T.; Henning, A.; Bissolo, M.; Zengerle, M.; Gregoratti, L.; Amati, M.; Zeller, P.; Eichhorn, J.; Stier, A. V.; Holleitner, A. W.; Finley, J. J.; Sharp, I. D. Real-Time Investigation of Sulfur Vacancy Generation and Passivation in Monolayer Molybdenum Disulfide via in Situ X-Ray Photoelectron Spectromicroscopy. *ACS Nano* **2022**, *16* (12), 20364−20375.
(46) Lainé, A.; Parmar, R.; Amati, M.; Gregoratti, L.; Su, G.; Xu, T.; Salmeron, M. Damage-Free X-Ray Spectroscopy Characterization of Oxide Thin Films. *Appl. Surf. Sci.* **2023**, *634*, No. 157335.
(47) Giannozzi, P.; Baroni, S.; Bonini, N.; Calandra, M.; Car, R.; Cavazzoni, C.; Ceresoli, D.; Chiarotti, G. L.; Cococcioni, M.; Dabo, I.; Dal Corso, A.; De Gironcoli, S.; Fabris, S.; Fratesi, G.; Gebauer, R.; Gerstmann, U.; Gougoussis, C.; Kokalj, A.; Lazzeri, M.; Martin-Samos, L.; Marzari, N.; Mauri, F.; Mazzarello, R.; Paolini, S.; Pasquarello, A.; Paulatto, L.; Sbraccia, C.; Scandolo, S.; Sclauzero, G.; Seitsonen, A. P.; Smogunov, A.; Umari, P.; Wentzcovitch, R. M. QUANTUM ESPRESSO: A Modular and Open-Source Software Project for Quantum Simulations of Materials. *J. Phys.: Condens. Matter* **2009**, *21* (39), No. 395502.
(48) Giannozzi, P.; Andreussi, O.; Brumme, T.; Bunau, O.; Buongiorno Nardelli, M.; Calandra, M.; Car, R.; Cavazzoni, C.; Ceresoli, D.; Cococcioni, M.; Colonna, N.; Carnimeo, I.; Dal Corso, A.; De Gironcoli, S.; Delugas, P.; Distasio, R. A.; Ferretti, A.; Floris, A.; Fratesi, G.; Fugallo, G.; Gebauer, R.; Gerstmann, U.; Giustino, F.; Gorni, T.; Jia, J.; Kawamura, M.; Ko, H. Y.; Kokalj, A.; Kücükbenli, E.; Lazzeri, M.; Marsili, M.; Marzari, N.; Mauri, F.; Nguyen, N. L.; Nguyen, H. V.; Otero-De-La-Roza, A.; Paulatto, L.; Poncé, S.; Rocca, D.; Sabatini, R.; Santra, B.; Schlipf, M.; Seitsonen, A. P.; Smogunov, A.; Timrov, I.; Thonhauser, T.; Umari, P.; Vast, N.; Wu, X.; Baroni, S. Advanced Capabilities for Materials Modelling with Quantum ESPRESSO. *J. Phys.: Condens. Matter* **2017**, *29* (46), No. 465901.
(49) Hamada, I. Van Der Waals Density Functional Made Accurate. *Phys. Rev. B: Condens. Matter Mater. Phys.* **2014**, *89* (12), No. 121103.
(50) van Setten, M. J.; Giantomassi, M.; Bousquet, E.; Verstraete, M. J.; Hamann, D. R.; Gonze, X.; Rignanese, G. M. The PSEUDODOJO: Training and Grading a 85 Element Optimized Norm-Conserving Pseudopotential Table. *Comput. Phys. Commun.* **2018**, *226*, 39−54.
(51) Henkelman, G.; Arnaldsson, A.; Jónsson, H. A Fast and Robust Algorithm for Bader Decomposition of Charge Density. *Comput. Mater. Sci.* **2006**, *36* (3), 354−360.
(52) Hamann, D. R. Optimized Norm-Conserving Vanderbilt Pseudopotentials. *Phys. Rev. B: Condens. Matter Mater. Phys.* **2013**, *88* (8), No. 085117.
(53) Pehlke, E.; Scheffler, M. Evidence for Site-Sensitive Screening of Core Holes at the Si and Ge (001) Surface. *Phys. Rev. Lett.* **1993**, *71* (14), 2338−2341.
(54) Campedelli, E.; Mazzucato, M.; Parnigotto, M.; Pedrielli, A.; Gatsios, C.; Badocco, D.; Pastore, P.; Timpel, M.; Nardi, M. V.; Durante, C. Ionized Jet Deposition of $MoS_2$ on Gas Diffusion Layer Electrodes for Next Generation Alkaline Electrolyzers. *Adv. Sustainable Syst.* **2025**, *9*, No. 2400979.

Downloaded from pubs.acs.org/aamick/article-pdf/18/30/41889/65852670/am-2026-04862n.pdf by POLITECNICO DI TORINO user on 22 October 2026


https://doi.org/10.1021/acsami.6c04862
ACS Appl. Mater. Interfaces 2026, 18, 41889−41902

(55) Gatensby, R.; McEvoy, N.; Lee, K.; Hallam, T.; Berner, N. C.; Rezvani, E.; Winters, S.; O'Brien, M.; Duesberg, G. S. Controlled Synthesis of Transition Metal Dichalcogenide Thin Films for Electronic Applications. *Appl. Surf. Sci.* **2014**, *297*, 139−146.

(56) Agrawal, A. V.; Polyakov, A. Y.; Eriksson, J.; Antosiewicz, T. J.; Shegai, T. O. Humidity-Enhanced $NO_2$ Gas Sensing Using Atomically Sharp Edges in Multilayer $MoS_2$. *Small Struct.* **2025**, *6* (4), No. 2400409.

(57) Agrawal, A. V.; Kumar, N.; Kumar, M. Strategy and Future Prospects to Develop Room-Temperature-Recoverable $NO_2$ Gas Sensor Based on Two-Dimensional Molybdenum Disulfide. *Nanomicro Lett.* **2021**, *13* (1), 38.

(58) Ashcroft, N. W.; Mermin, N. D. *Solid State Physics*; Saunders College Publishing, **1976**.

(59) Böttcher, S.; Vita, H.; Horn, K. Reversible Photon-Induced Oxidation of Graphene by $NO_2$ Adsorption. *Surf. Sci.* **2014**, *621*, 117−122.

(60) Piancastelli, M. N.; Carravetta, V.; Hjelte, I.; De Fanis, A.; Okada, K.; Saito, N.; Kitajima, M.; Tanaka, H.; Ueda, K. Experimental and Theoretical Study of Resonant Auger Decay of Core-Excited $NO_2$. *Chem. Phys. Lett.* **2004**, *399* (4−6), 426−432.

(61) Yamazaki, M.; Adachi, J.-I.; Kimura, Y.; Stener, M.; Decleva, P.; Yagishita, A. N 1s Photoelectron Angular Distributions from Fixed-in-Space $NO_2$ Molecules: Stereodynamics and Symmetry Considerations. *J. Chem. Phys.* **2010**, *133* (16), No. 164301.

(62) Grell, G.; Bokarev, S. I. Multi-Reference Protocol for (Auto)Ionization Spectra: Application to Molecules. *J. Chem. Phys.* **2019**, *152* (7), No. 074108.

Downloaded from pubs.acs.org/aamick/article-pdf/18/30/41889/65852670/am-2026-04862n.pdf by POLITECNICO DI TORINO user on 22 October 2026



https://doi.org/10.1021/acsami.6c04862
*ACS Appl. Mater. Interfaces* 2026, 18, 41889−41902